photonics

MDPI

Communication

In Vivo Rodent Cervicothoracic Vasculature Imaging Using Photoacoustic Computed Tomography

Junsoo Lee [1], Hoseong Cho [1], Sungjo Park [2], Jaeyul Lee [3], Daewoon Seong [1], Ruchire Eranga Wijesinghe [4], Sangyeob Han [5], Shinheon Kim [5], Mansik Jeon [1] and Jeehyun Kim [1,*]

1 School of Electronic and Electrical Engineering, Kyungpook National University, Daegu 41566, Korea; jslee5399@knu.ac.kr (J.L.); ghtjd419@knu.ac.kr (H.C.); smc7095@knu.ac.kr (D.S.); msjeon@knu.ac.kr (M.J.)
2 Pohang Innotown Center, Pohang University of Science and Technology, Pohang 37673, Korea; psj2686@postech.ac.kr
3 Department of Bioengineering, University of California, Los Angeles, CA 90095, USA; jaeyul21@g.ucla.edu
4 Department of Materials and Mechanical Technology, Faculty of Technology, University of Sri Jayewardenepura, Pitipana, Homagama 10200, Sri Lanka; erangawijesinghe@sjp.ac.lk
5 Institute of Biomedical Engineering, Kyungpook National University, Daegu 41566, Korea; syhan850224@knu.ac.kr (S.H.); shawnkim@knu.ac.kr (S.K.)
* Correspondence: jeehk@knu.ac.kr; Tel.: +82-53-950-7221

Abstract: Mice and rats are rodent specimens commonly used in multidisciplinary research. Specifically, vasculature imaging of rodents has been widely performed in preclinical studies using various techniques, such as computed tomography, magnetic resonance imaging, and ultrasound imaging. Photoacoustic CT (PACT) is a noninvasive, nonionizing optical imaging technique derived from photoacoustic tomography and benefits from using intrinsic endogenous contrast agents to produce three-dimensional volumetric data from images. In this study, a commercial PACT device was employed to assess the cervicothoracic vasculature of mouse and rat specimens, which has rarely been examined using PACT, under two conditions with depilation and skin incision. Various blood vessels, including the common carotid artery, internal/external jugular veins, cranial vena cava, internal thoracic vein, and mammary, were identified in the acquired PACT images. The difference between the depilated and skin-incised specimens also revealed the presence of branches from certain blood vessels and specific anatomical features such as the manubrium of the sternum. This study presents detailed PACT images observing the cervicothoracic vasculature of rodent specimens and is expected to be used as a reference for various preclinical experiments on mice and rats.

Keywords: rodent; small animal; vascular imaging; angiography; photoacoustic imaging; photoacoustic computed tomography; cervicothoracic vasculature

Citation: Lee, J.; Cho, H.; Park, S.; Lee, J.; Seong, D.; Wijesinghe, R.E.; Han, S.; Kim, S.; Jeon, M.; Kim, J. In Vivo Rodent Cervicothoracic Vasculature Imaging Using Photoacoustic Computed Tomography. *Photonics* **2021**, *8*, 312. https://doi.org/10.3390/photonics8080312

Received: 30 June 2021
Accepted: 2 August 2021
Published: 3 August 2021

1. Introduction

In scientific research, rodents (also called murine) have been widely used for animal tests and experiments. Specifically, mice and rats are the most commonly used species owing to their easy handling, high reproduction rate, and low cost [1]. Studies and applications using mice or rats are abundantly available and vary between academic fields, such as biology [2–4], medicine [5–8], psychology [9–11], and other disciplines [12–14]. The morphologies of rodents from anatomical information, including osteology, arthrology, myology, and various organs and systems, have been fundamental references for experiments using rodent specimens [15]. In particular, rodents have been utilized in preclinical research and studies in biomedical engineering because of their similarities and analogous features with humans in terms of not only molecular mechanisms but also systemic physiology to disease pathogenesis based on metabolic homogeneities [16,17].

Although the basic physiological structures and forms of murine are similar to those of humans, several morphological differences occur in the sizes and volumes of the organs

depending on their functions [18,19]. One of the examples of morphological differences between humans and rodents is in the vasculature. In humans, the blood vessels to the central nervous system are thicker because of the high demand for oxygen and nutrients, whereas rodents have thicker blood vessels connected to other sensory sites such as the facial area. This difference is evident in the thicknesses of the external and internal jugular veins (EJVs and IJVs); in humans, the IJVs are thicker than the EJVs, whereas this is opposite in rodents [4]. Therefore, the availability of rodent vascular images for reference can help prevent errors during preclinical experiments where the hypotheses and goals of the studies are based on the human vascular structure. In addition, certain intricate branches of the blood vessels can be identified by in vivo vascular imaging, which is hard to preserve during dissections for visual inspection. Hence, in vivo vascular imaging of rodents can guide multidisciplinary research when using rodent specimens.

Conventional imaging techniques for small-animal vascular imaging (angiography) include computed tomography (CT), magnetic resonance imaging (MRI), and ultrasonic (US) imaging. Through CT angiography procedures, such as the micro-CT angiogram, the vasculatures of small-animal samples can be imaged as volumetric data with high spatial resolutions of the order of 30 μm to 100 μm by in vivo micro-CT imaging and from 1 μm to 30 μm by ex vivo imaging [20]. However, radiopaque compounds, such as silicon rubber compound, need to be injected into the blood vessels for high-resolution imaging [21], with unavoidable radiation exposure thereafter [22]. On the other hand, contrast-enhanced magnetic resonance angiography (CE-MRA), which is derived from MRI, has the advantages of imaging via the intrinsic magnetic properties of the blood and tissues and does not involve ionizing radiation [23]. CE-MRA can provide spatial resolutions of the order of 1 mm to 4 mm with acquisition times of around 30 s [24]. Although CE-MRA has the advantages of low cost and reduced imaging time compared to conventional catheter angiography, the use of gadolinium-based contrast agents, which can cause allergic reactions, and insufficient resolution for small-vascular imaging are significant limitations [25]. High-frequency color Doppler US imaging has been shown to compensate for the limitations of using contrast agents and ionizing radiation in CT angiography and CE-MRA, with axial resolutions of up to 90 μm [21,26,27]. Nonetheless, this technique has the disadvantage of a restricted ability to produce tomographic images; the inclination to interpret the obtained images based on subjective analyses by the operators is another limitation [28]. Thus, vascular imaging techniques with noninvasive and nonionizing volumetric imaging capabilities free of contrast materials are in demand.

Optical imaging techniques, such as optical coherence tomography (OCT) and photoacoustic tomography (PAT), have attracted attention due to their noninvasive and nonionizing tomographic and volumetric imaging capabilities. OCT is an interferometric optical imaging technique that uses a broadband light source to generate micrometer-scaled tomography [29]. Among OCT techniques, OCT-Angiography (OCTA) can produce high-resolution vascular images without contrast agents [30,31]. However, OCTA has a limitation of less than 2 mm of penetration depth [32].

PAT is another noninvasive optical imaging technique using a pulsed laser and US transducer with a penetration depth of up to several centimeters [33,34]. The basic principle of PAT imaging involves capturing acoustic signals generated by the intrinsic endogenous contrast materials of specimens, which can be induced by thermoelastic expansion after light absorption. PAT imaging can be used to examine the vasculature of a specimen through volumetric and tomographic images with penetration depths in the order of several millimeters and resolution ranging from several micrometers to millimeters, depending on the system configuration [35,36]. PAT has been actively utilized to image the vasculature of small animals, including rodents. However, most of the previous studies using PAT have involved intensive imaging of specific sites, such as tumors, cancer cell lesions, and the brain, or observing the changes in photoacoustic (PA) signal amplitudes from various regions of interest (ROIs) after injecting exogenous contrast agents [37–40]. Whole-body

PAT imaging has also been studied over the past few years, but the acquired vascular images were at the macroscopic level [41,42].

Photoacoustic computed tomography (PACT) is one of the PAT methods that use multiple US transducers or ring-type transducer arrays rather than a single transducer with point scanning [43,44]. Recently, various PACT devices have been developed and commercially introduced [45]. In the present study, a commercial PACT instrument was used to image the vasculatures of mouse and rat specimens from the cervicothoracic region, which has been infrequently investigated using PACT. For each of the commonly used rodent specimens (mouse and rat), the various blood vessels in the thorax, such as the common carotid artery (CCA), EJV/IJV, subclavian vein (SV), and cranial vena cava (CVC), were identified from the acquired PACT volumetric images without any contrast agents. In addition, the differences in the PACT images of the thoracic regions between depilated and skin-incised conditions of each of the specimens were presented. Thus, the methods and results of this study can be utilized as references for the cervicothoracic vasculatures of mice and rats in various preclinical experiments.

2. Materials and Methods

2.1. Photoacoustic Computed Tomography Scanner

The PACT scanner used in this study is a commercial instrument, having a total of 128 US transducers to record acoustic signals from the specimens when induced by an Nd:YAG nanosecond pulsed laser (Nexus 128, Endra Life Science Inc., Ann Arbor, MI, USA) [46]. A schematic of the scanner part of the instrument is presented, along with photographs of the device, in Figure 1. The physical dimensions of the device are 0.9 × 0.7 × 1.1 m (W × D × H). The light input used for PACT imaging was generated using an Nd:YAG pulsed laser of wavelength 532 nm and transmitted to a tunable optical parametric oscillator (OPO), which is a coherent light source based on parametric amplification through a nonlinear crystal and generate multiple light fields due to variances in the crystal's refractive index [47]. The tuning range for the wavelength of output light is 680–950 nm. The light output energy was approximately 6 mJ/pulse, which adheres to the American National Standards Institute (ANSI) limits. The repetition rate of the laser was 20 Hz, and the single laser shot in every 1.5° step was recorded during the scanner rotated at the speed of 30°/s. The total scanning time for 360° took 12 s in the continuous rotation acquisition mode. A total of 128 unfocused US transducers with center frequencies of 5 MHz and diameters of 3 mm were embedded in a round bowl-shaped rotating mount. This instrument provided a spatial resolution of <280 μm and a field of view (FOV) exceeding 20 mm. Deionized (DI) water was filled in the rotating mount, and the temperature of the DI water was maintained at 37 ± 0.5 °C consistently using a temperature controller. This temperature setting was followed by the guideline of the PACT device manual and the previous study by Hu et al. for photoacoustic imaging of small animals [48]. Between the rodent specimen and the tray floor, US gel was applied as a medium for transmitting the acoustic signals. The top lid had a small hole for the anesthetic gas tube (yellow line) and a vision camera to check the respiratory status of the specimen during PACT imaging. The PACT data were acquired and reconstructed by a multi-core processor personal computer (PC), and viewing and analysis of the three-dimensional (3D) anatomical volume data were accomplished through digital imaging and communications in medicine (DICOM) image processing application (OsiriX Lite, Pixmeo SARL, Switzerland) [49]. The PC for data acquisition and the DICOM image processing application were provided by Endra Life Science Inc. when purchasing the PACT device.

Although the PACT device offers various wavelengths of the laser with a tuning range of 680–950 nm, in this study, the wavelength of the laser light from the OPO was fixed at 800 nm to acquire cervicothoracic vasculature images of both the arteries and veins because the molar extinction coefficients of both oxyhemoglobin (HbO_2) and deoxyhemoglobin (Hb) are 0.20 $mM^{-1} \cdot cm^{-1}$ at 800 nm [50].

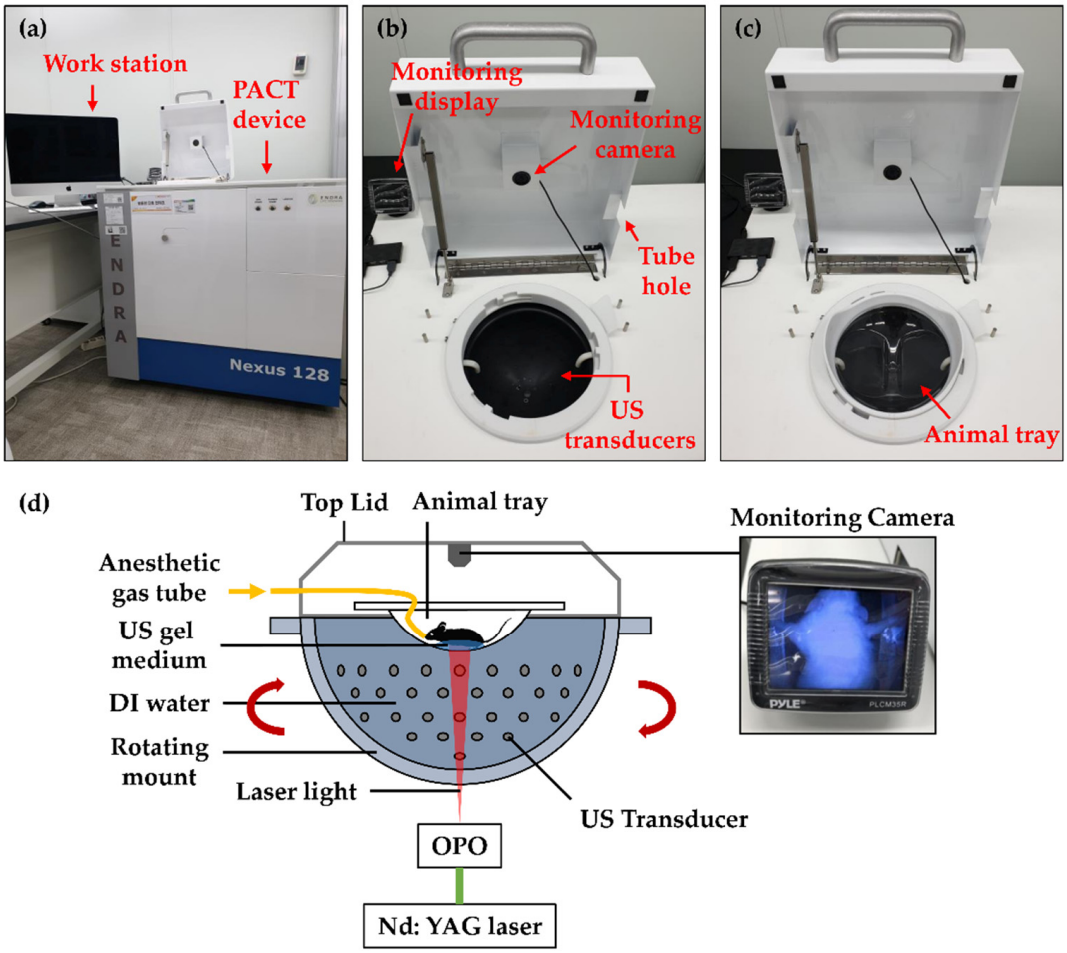

Figure 1. Photographs and schematic of the PACT device. Photographs include (**a**) overall system, (**b**) scanner part before installing the animal tray, and (**c**) scanner part with the animal tray. (**d**) Diagram of the PACT scanner; the mechanical parts, including the motor system of the rotating mount, are not shown; The photograph of the monitoring camera displays the external output from the vision camera and shows a rat specimen in the dorsal view.

2.2. Rodent Specimen Imaging

The animal experiments in this study were performed in compliance with the protocols and guidelines approved by the Institutional Animal Care and Use Committee of Kyungpook National University (permission number of KNU-2018-100). The two rodent specimens used in this study were a female BALB/c mouse (age: 5–6 weeks; body weight: 20–25 g) and a female Sprague–Dawley rat (age: 4–5 weeks; body weight: 200–250 g). For the PACT imaging, the specimens were placed in a nose cone with a tube for inhalation of isoflurane gas as the anesthetic agent (3% for induction and 1.5% for maintenance in pure oxygen). Then, a depilatory cream was gently applied to the thorax for 2 min and carefully wiped using wet gauze for hair removal (Nair®, Church and Dwight Co., Inc., Ewing, NJ, USA). Prior to positioning the specimen on the tray, the temperature of the DI water inside the rotating mount was set to a sufficient temperature (37 °C). The US gel was spread in a layer of thickness 20 mm, and adequate space was secured to ensure the respiratory requirements of the specimen.

After PACT imaging of the depilated specimen, the pelt on the area over the thorax was carefully incised to confirm the observed vasculature. Prior to incision, the thoracic area was gently wiped with a gauze doused in 70% ethanol to prevent contamination. Using forceps, the external skin layer and fur were pinched and held. The anesthetic status of the specimen was continuously monitored, while a ventral incision was cautiously made using fine straight and curved scissors. Then, PACT imaging was repeated for

the specimens in the skin-incised cervicothoracic region. Finally, the specimens were euthanized by cervical dislocation, and the rib cages of the specimens were cut using bone scissors to verify specific blood vessels such as the internal thoracic vein. Unnecessary incision or abuse of dissection was avoided during the entire experimental process.

3. Results

During the experiment, the anesthetized and depilated specimens were carefully placed on the imaging window located at the middle bottom of the animal tray. PACT images for each specimen were then acquired using only the endogenous intrinsic contrast at a single wavelength (800 nm) with a FOV of 25.4 mm × 25.4 mm. The scanning mode was a step-and-shoot rotation acquisition (Number of Angles: 360; Number of Pulses per Angle: 10), which took a total of 4 min for 360° scan and data processing.

3.1. PACT Images of Rodent Specimens after Depilation

The upper thorax of the rat specimen around the clavicle was imaged using the instrument. Figure 2 shows the imaging area indicated by the red box for the ventral view (a) and the acquired PACT images from three different directions (b–d). Through the PACT images, specific arteries and veins, such as the CCA, IJV and EJV, SV, and CVC, were observed, and several branches beneath the skin surface were displayed. In particular, the junction (brachiocephalic vein) connecting the right EJV, SV, and CVC was obviously seen, and the CCA and IJV were distinguished well (yellow-dashed ellipse). On the lateral view image in Figure 2d, the superficial branches (green arrows) were identified, and the depth of the aforementioned junction was estimated as 4.58 mm from the skin surface (yellow double-headed arrow). The 3D volumetric video clip of the PACT image for Figure 2 is shown in Video S1.

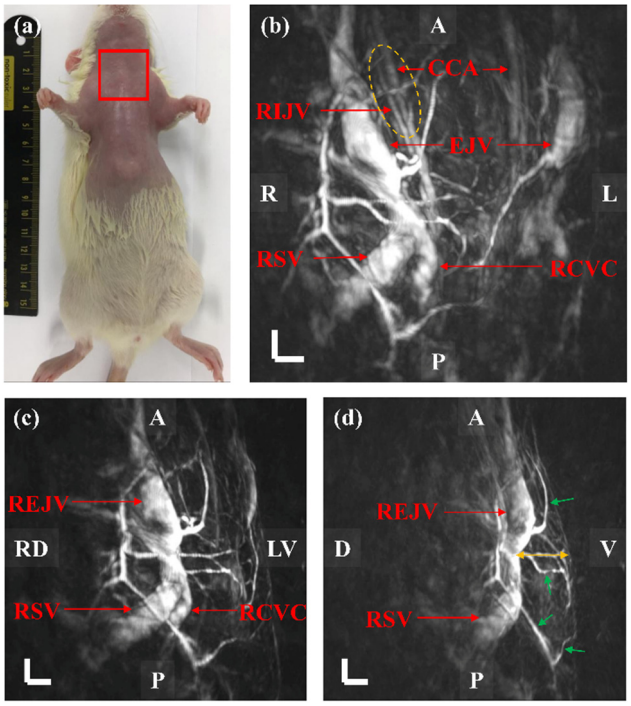

Figure 2. Photograph of the depilated rat specimen and its PACT images. (**a**) Photograph of the specimen showing the imaging region (red box). (**b**) Ventral view of the PACT image; the yellow-dashed ellipse shows the CCA and IJV distinctly. (**c**) Right ventral view of the PACT image. (**d**) Right lateral view of the PACT image; the yellow double-headed arrow indicates the depth of the junction (4.58 mm), and the green arrows indicate the superficial branches. A: anterior, CCA: common carotid artery, D: dorsal, EJV: external jugular vein, L: left, LV: left ventral, P: posterior, R: right, RCVC: right cranial vena cava, RD: right dorsal, REJV: right external jugular vein, RIJV: right internal jugular vein, RSV: right subclavian vein, V: ventral. Scale bar: 2 mm.

During PACT imaging of the mouse specimen, the thorax from the clavicle to xiphoid cartilage, which is located at the end of the sternebrae, was included in the FOV (25.4 mm × 25.4 mm). Figure 3 shows the ventral view of the specimen with the imaging region (a) and acquired PACT images (b–d). In addition to the EJV, CVC, and SV, more blood vessels, such as the right and left mammary (RM and LM) vessels, superficial thoracic vein (STV), internal thoracic vein (ITV), and superior epigastric vein (SEV), are visible from the PACT images. In Figure 3b, which is the ventral view, the RM and LM vessels are observed to extend from the top to the bottom on both sides, and the two ITVs on the left and right sides of the sternebrae are clearly identified with high intensity. On the lateral view PACT image (Figure 3d), the location of ITV, which is just below the costal cartilage, was confirmed. The volumetric image of Figure 3 is shown in Video S2.

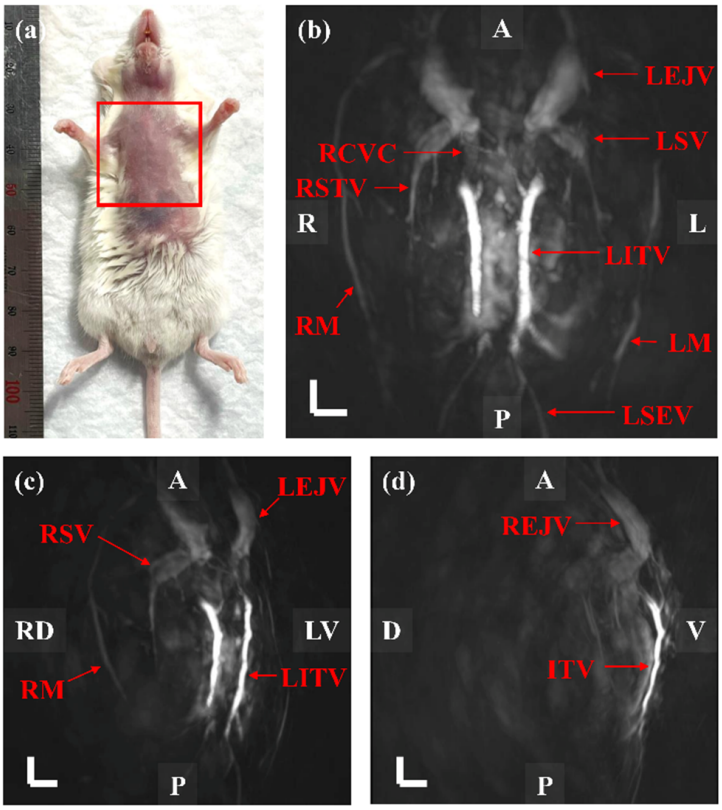

Figure 3. Photograph of the depilated mouse specimen and its PACT images. (**a**) Photograph of the specimen showing the imaging region (red box). (**b**) Ventral view PACT image. (**c**) Right ventral view PACT image. (**d**) Right lateral view PACT image. A: anterior, D: dorsal, ITV: internal thoracic vein, L: left, LEJV: left external jugular vein, LITV: left internal thoracic vein, LM: left mammary, LSEV: left superior epigastric vein, LSV: left subclavian vein, LV: left ventral, P: posterior, R: right, RCVC: right cranial vena cava, RD: right dorsal, REJV: right external jugular vein, RM: right mammary, RSTV: right superficial thoracic vein, RSV: right subclavian vein, V: ventral. Scale bar: 2 mm.

To confirm the locations of the blood vessels seen on the acquired PACT images, an incision was made on the thoracic skin of the mouse specimen. Figure 4 shows the representative ventral view PACT image of the specimen (a), photographs taken after skin incision (b and c), and a photograph showing the backside of a rib after euthanasia (d). The EJV and SEV were well matched with those on the PACT image, and the RM was located beneath the skin in an identical shape to that on the PACT image. On the backside of the rib, the left and right ITVs were observed next to the sternebrae. The remaining arteries and veins observed on the PACT images, such as the CCA, IJV, SV, and CVC, were difficult to confirm owing to hemorrhage during the dissection.

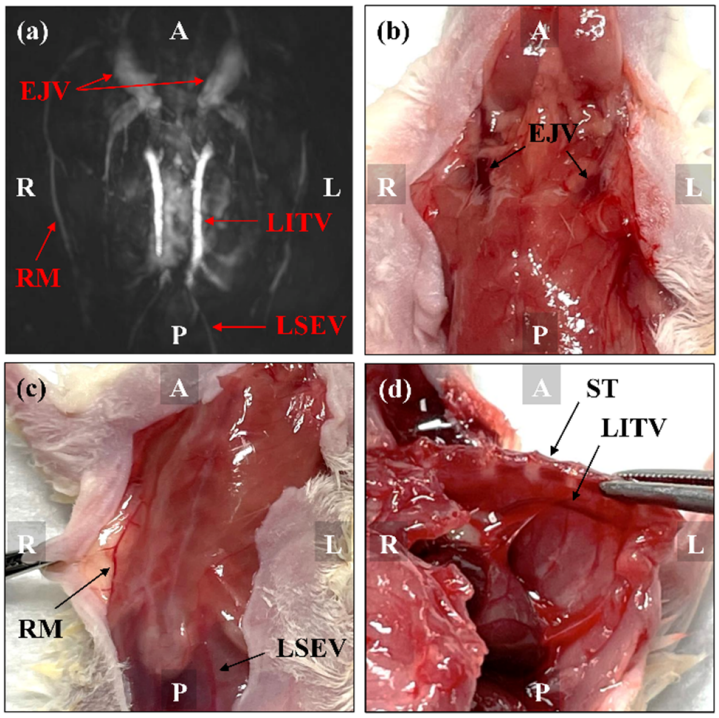

Figure 4. Visual confirmation of the imaged blood vessels via skin incision and dissection. (**a**) Representative PACT image of the ventral side of the mouse specimen. (**b**,**c**) Photographs of the thorax of the mouse specimen after skin incision. (**d**) Photograph of the backside of the rib. A: anterior, EJV: external jugular vein, L: left, LITV: left internal thoracic vein, LSEV: left superior epigastric vein, P: posterior, R: right, RM: right mammary, ST: sternebrae.

3.2. PACT Images after Skin Incision

After performing the skin incision, each rodent specimen was imaged again in the cervicothoracic region. The FOV, scanning mode, and wavelength of light were maintained the same as before, i.e., 25.4 mm × 25.4 mm, step-and-shoot rotation acquisition, and 800 nm, respectively.

Figure 5 shows the PACT images of the rat specimen. The imaged region was the neck area from the chin to the clavicle. Because of the skin incision, the branches of the blood vessels around the EJV and CCA, which were seen in the PACT image after depilation (Figure 1), disappeared noticeably. Therefore, differentiation between the CCA and IJV was more apparent, and the EJV was clearly displayed. One of the branches (yellow arrow) next to the right CCA remained, and its location was confirmed as the topmost surface in the lateral view image (Figure 5c). The unwanted signal in the image is blood clots in the US gel, which detached during positioning of the specimen. The 3D video clip of Figure 5 is shown in Video S3.

The procedures and settings detailed above were used to acquire the PACT images of the skin-incised mouse specimen. Figure 6 shows the PACT image of the specimen in three views. The imaged region included the thorax from the chin to ribs. Although the photoacoustic signal amplitude at the center of the thorax was saturated, the Y-shaped manubrium of the sternum (MoS) and blood vessels, including the EJV, CCA, and ITV, could be identified. The saturated signals in the middle of the figure are handled as noted later in the discussion. From the lateral view image (Figure 6c), the depth positions of the MoS and ITV were confirmed to correspond to the region below the surface of the fascia. The video for this volumetric image is shown in Video S4.

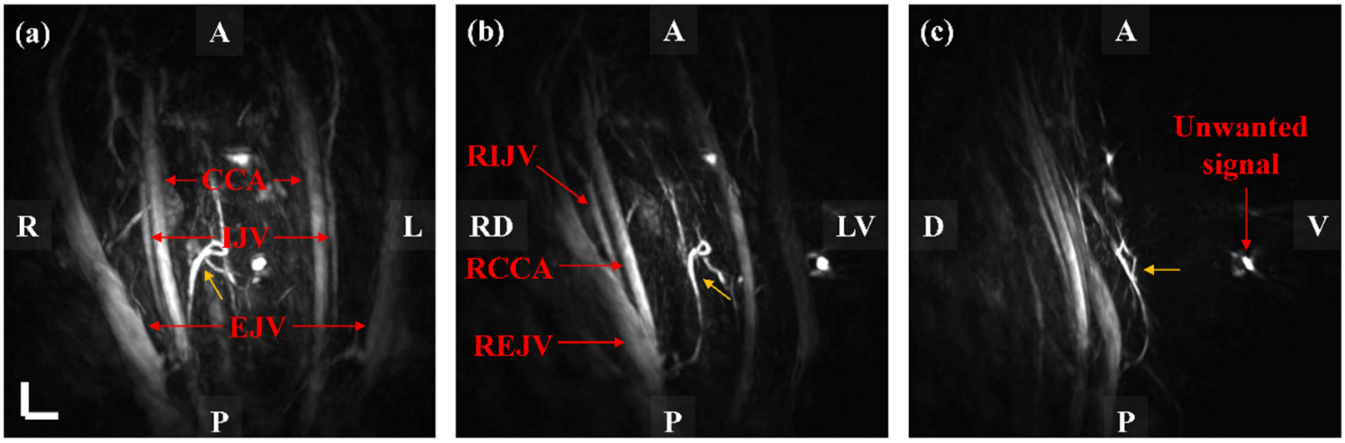

Figure 5. PACT images of the rat specimen after skin incision. (**a**) Ventral view PACT image. (**b**) Right ventral view PACT image. (**c**) Right lateral view PACT image. The yellow arrows indicate the remaining branches on the surface. A: anterior, CCA: common carotid artery, D: dorsal, EJV: external jugular vein, IJV: internal jugular vein, L: left, LV: left ventral, P: posterior, R: right, RCCA: right common carotid artery, RD: right dorsal, REJV: right external jugular vein, RIJV: right internal jugular vein, V: ventral. Scale bar: 2 mm.

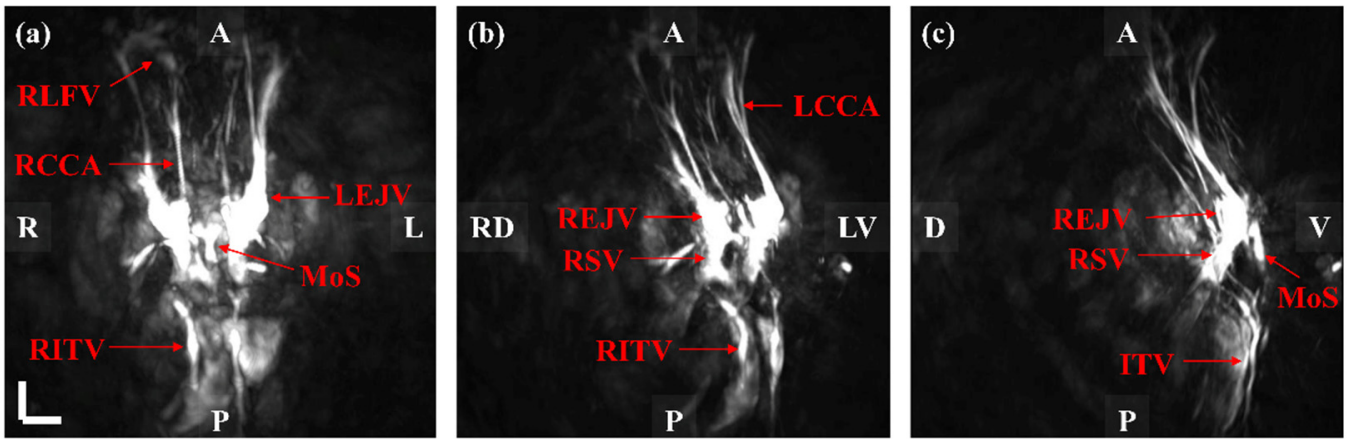

Figure 6. PACT images of the mouse specimen after skin incision. (**a**) Ventral view PACT image. (**b**) Right ventral view PACT image. (**c**) Right lateral view PACT image. A: anterior, D: dorsal, ITV: internal thoracic vein, L: left, LCCA: left common carotid artery, LEJV: left external jugular vein, LV: left ventral, MoS: manubrium of the sternum, P: posterior, R: right, RCCA: right common carotid artery, RD: right dorsal, REJV: right external jugular vein, RITV: right internal thoracic vein, RLFV: right linguofacial vein, RSV: right subclavian vein, V: ventral. Scale bar: 2 mm.

4. Discussion

This study uses a commercial noninvasive and nonionizing optical imaging instrument called PACT to obtain the cervicothoracic vasculature images of mouse and rat specimens, which are some of the most commonly used experimental animals in academic research. The acquired PACT images of each of the specimens revealed various blood vessels of the cervicothoracic region and thorax (in the case of the mouse specimen), such as the common carotid artery, external/internal jugular vein, cranial vena cava, subclavian vein, superficial thoracic vein, internal thoracic vein, right/left mammary, and superior epigastric vein. The PACT images obtained after skin incisions showed that several branches of the blood vessels had collapsed. Specific blood vessels, including the external jugular, mammary, and internal thoracic veins, were confirmed via dissection. Previous works reported in the literature for rodent anatomy were also referred to identify the blood vessels from the obtained PACT images [15,51].

The results of this study confirm the vascular information from the upper thoracic parts (cervicothoracic regions) of mice and rats, which have been infrequently observed through PACT imaging. Moreover, the different conditions of the specimens after depilation and skin incision implemented in this study have not been considered much to date. Therefore, this study is expected to guide PACT imaging of mouse and rat specimens for the thoracic region and be utilized as a reference for the cervicothoracic vasculature in various preclinical experiments using mice and rats.

The commercial PACT instrument employed in this study (Nexus 128, Endra Life Science Inc., Ann Arbor, MI, USA) was easy to use and produced sufficiently clear PACT images to identify the significant blood vessels. The components for animal handling, including the animal tray, CCD monitoring camera, and hole in the top lid for the anesthetic gas tube, are convenient to handle small animal specimens, compared to conventional laboratory-based PACT systems that require the effort to mount small animals to an animal holder and to fix the anesthetic gas tube to the nasal part of the specimen. Nexus 128 also has the practical advantage of obtaining data through the provided software that performs from image acquisition to image processing and displaying. However, several limitations are noted. Because the scanning area (i.e., FOV) was fixed (>20 mm), the range covering the thoracic region of each specimen in the PACT images was different. Further, the animal tray used to position the specimens was a little small to mount a four-week-old rat. Another limitation of the instrument was that the output laser was slightly focused on a certain depth in the middle of the animal tray, causing unwanted strong acoustic signals (Figure 6). Hence, improvements to the system are required for the abovementioned shortcomings, and modifications of the configuration related to the pulsed laser and US transducers can help achieve better spatial resolution.

While this study proposes the anatomical vascular information according to the two commonly used small animals (mice and rats) and different dissection statuses, the capabilities of the device for quantitative analyses, such as parametric maps of hemoglobin concentration (C_{Hbt}), line measurement, and image statistics, can be utilized for various future preclinical studies. Blood oxygen saturation (SaO_2), which can be calculated by PACT data acquired at multiple wavelengths, is also helpful for versatile biomedical applications [52]. In addition, the PACT images can be improved and used as functional imaging when using exogenous contrast agents such as dye and nanoparticles. Hu et al. developed lysosome-targeting BODIPY nanoparticles for enhancing lysosomal photoacoustic imaging (PAI) [53], and Temma et al. utilized a novel cyanine dye IC7-1-Bu as a PAI contrast agent for in vivo tumor imaging [54]. Along with the system improvements and the use of contrast agents, several future studies are proposed as follows: observing and analyzing the vasculature of other representative rodents such as guinea pigs using PACT, imaging different body parts, and investigating differences in PACT images according to the dissection stages or anatomical conditions.

5. Conclusions

In this study, a commercial PACT device (Nexus 128, Endra Life Science Inc., Ann Arbor, MI, USA) was used to acquire the cervicothoracic vasculature images of commonly used small animals (mouse and rat) noninvasively. A wavelength of 800 nm and a field of view (FOV) of 25.4 mm × 25.4 mm were applied during the experiment. The total amount of time consumed to acquire PACT data and image processing was 4 min. The presented PACT images from the cervicothoracic region of mouse and rat specimen show anatomical features of various blood vessels, including the common carotid artery, cranial vena cava, subclavian vein, external/internal jugular vein, superficial thoracic vein, internal thoracic vein, superior epigastric vein, and right/left mammary. According to the two statuses of depilation and skin incision, the branches of the blood vessels and structural differences in PACT images are also revealed. This study is expected to guide the PACT imaging of small animals for the thoracic region and be utilized to reference the cervicothoracic vasculature in various preclinical experiments using mice and rats.

Supplementary Materials: The following are available online at https://www.mdpi.com/article/10.3390/photonics8080312/s1, Video S1: PACT volumetric image of the depilated rat specimen. Video S2: PACT volumetric image of the depilated mouse specimen. Video S3: PACT volumetric image of the skin-incised rat specimen. Video S4: PACT volumetric image of the skin-incised mouse specimen.

Author Contributions: Conceptualization, S.P. and M.J.; methodology, S.P.; software, H.C.; validation, J.L. (Junsoo Lee), S.P., and J.K.; formal analysis, J.L. (Junsoo Lee) and H.C.; investigation, D.S. and J.L. (Jaeyul Lee); resources, S.P. and M.J.; data curation, J.L. (Junsoo Lee) and S.K.; writing—original draft preparation, J.L. (Junsoo Lee); writing—review and editing, R.E.W.; visualization, J.L. (Junsoo Lee); supervision, J.K.; project administration, S.P. and M.J.; funding acquisition, M.J. and S.H. All authors have read and agreed to the published version of the manuscript.

Funding: This research was supported by the Kyungpook National University Development Project Research Fund, 2018. This research was also supported by the Basic Science Research Program through the National Research Foundation of Korea (NRF), funded by the Ministry of Education (No. 2018R1D1A1B07043340 and 2020R1I1A1A01072399).

Institutional Review Board Statement: The study was conducted according to the guidelines of the Declaration of Helsinki and approved by the Institutional Animal Care and Use Committee of Kyungpook National University (permission number of KNU-2018-100).

Informed Consent Statement: Not applicable.

Data Availability Statement: The data presented in this study are available on request from the corresponding author.

Conflicts of Interest: The authors declare no conflict of interest.

References

1. Bryda, E.C. The Mighty Mouse: The Impact of Rodents on Advances in Biomedical Research. *Mol. Med.* **2013**, *110*, 207–211.
2. Silver, L.M.; Abbott, C. Mouse Genetics: Concepts and Applications. *Genet. Res.* **1996**, *68*, 183.
3. Fox, J.G.; Barthold, S.; Davisson, M.; Newcomer, C.E. *The Mouse in Biomedical Research: Normative Biology, Husbandry, and Models*; Elsevier: San Diego, CA, USA, 2006; Volume 3.
4. Treuting, P.M.; Dintzis, S.M.; Liggitt, D.; Frevert, C.W. *Comparative Anatomy and Histology: A Mouse and Human Atlas (Expert Consult)*; Academic Press: London, UK, 2011.
5. Labrijn, A.F.; Meesters, J.I.; Bunce, M.; Armstrong, A.A.; Somani, S.; Nesspor, T.C.; Chiu, M.L.; Altintaş, I.; Verploegen, S.; Schuurman, J.; et al. Efficient Generation of Bispecific Murine Antibodies for Pre-Clinical Investigations in Syngeneic Rodent Models. *Sci. Rep.* **2017**, *7*, 2476. [CrossRef]
6. Goffinet, C.; Schmidt, S.; Kern, C.; Oberbremer, L.; Keppler, O.T. Endogenous CD317/Tetherin Limits Replication of HIV-1 and Murine Leukemia Virus in Rodent Cells and Is Resistant to Antagonists from Primate Viruses. *J. Virol.* **2010**, *84*, 11374–11384. [CrossRef]
7. Li, M.; Tang, Z.; Zhang, D.; Sun, H.; Liu, H.; Zhang, Y.; Zhang, Y.; Chen, X. Doxorubicin-Loaded Polysaccharide Nanoparticles Suppress the Growth of Murine Colorectal Carcinoma and Inhibit the Metastasis of Murine Mammary Carcinoma in Rodent Models. *Biomaterials* **2015**, *51*, 161–172. [CrossRef] [PubMed]
8. Rocco, M.L.; Balzamino, B.O.; Passeri, P.P.; Micera, A.; Aloe, L. Effect of Purified Murine NGF on Isolated Photoreceptors of a Rodent Developing Retinitis Pigmentosa. *PLoS ONE* **2015**, *10*, e0124810. [CrossRef]
9. Pedersen, C.S.; Sørensen, D.B.; Parachikova, A.I.; Plath, N. PCP-Induced Deficits in Murine Nest Building Activity: Employment of an Ethological Rodent Behavior to Mimic Negative-like Symptoms of Schizophrenia. *Behav. Brain Res.* **2014**, *273*, 63–72. [CrossRef]
10. Bell, R.; Hobson, H. 5-HT1A Receptor Influences on Rodent Social and Agonistic Behavior: A Review and Empirical Study. *Neurosci. Biobehav. Rev.* **1994**, *18*, 325–338. [CrossRef]
11. Holly, K.S.; Orndorff, C.O.; Murray, T.A. MATSAP: An Automated Analysis of Stretch-Attend Posture in Rodent Behavioral Experiments. *Sci. Rep.* **2016**, *6*, 31286. [CrossRef] [PubMed]
12. Choi, S.Y.; Saravia-Butler, A.; Shirazi-Fard, Y.; Leveson-Gower, D.; Stodieck, L.S.; Cadena, S.M.; Beegle, J.; Solis, S.; Ronca, A.; Globus, R.K. Validation of a New Rodent Experimental System to Investigate Consequences of Long Duration Space Habitation. *Sci. Rep.* **2020**, *10*, 2336. [CrossRef]
13. Balci, F.; Freestone, D.; Gallistel, C.R. Risk Assessment in Man and Mouse. *Proc. Natl. Acad. Sci. USA* **2009**, *106*, 2459–2463. [CrossRef] [PubMed]
14. Paul, L.; Miley, W.M.; Baenninger, R. Mouse Killing by Rats: Roles of Hunger and Thirst in Its Initiation and Maintenance. *J. Comp. Physiol. Psychol.* **1971**, *76*, 242–249. [CrossRef] [PubMed]
15. Ruberte, J.; Carretero, A.; Navarro, M. *Morphological Mouse Phenotyping: Anatomy, Histology and Imaging*; Elsevier: Madrid, Spain, 2017.

16. Demetrius, L. Of Mice and Men. *EMBO Rep.* **2005**, *6*, S39–S44. [CrossRef] [PubMed]
17. Schroeder, H.W. Similarity and Divergence in the Development and Expression of the Mouse and Human Antibody Repertoires. *Dev. Comp. Immunol.* **2006**, *30*, 119–135. [CrossRef] [PubMed]
18. Kuhlencordt, F.; Kruse, H.-P. Calcium Metabolism, Bone and Metabolic Bone Diseases. In *Proceedings of the 10th European Symposium on Calcified Tissues, Hamburg, Germany, 16–21 September 1973*; Springer Science & Business Media: Hamburg, Germany, 2012.
19. Shawber, C.J.; Kitajewski, J. Notch Function in the Vasculature: Insights from Zebrafish, Mouse and Man. *BioEssays* **2004**, *26*, 225–234. [CrossRef] [PubMed]
20. Zagorchev, L.; Oses, P.; Zhuang, Z.W.; Moodie, K.; Mulligan-Kehoe, M.J.; Simons, M.; Couffinhal, T. Micro Computed Tomography for Vascular Exploration. *J. Angiogenes Res.* **2010**, *2*, 7. [CrossRef] [PubMed]
21. Mancini, M.; Greco, A.; Tedeschi, E.; Palma, G.; Ragucci, M.; Bruzzone, M.G.; Coda, A.R.D.; Torino, E.; Scotti, A.; Zucca, I.; et al. Head and Neck Veins of the Mouse. A Magnetic Resonance, Micro Computed Tomography and High Frequency Color Doppler Ultrasound Study. *PLoS ONE* **2015**, *10*, e0129912. [CrossRef]
22. Boone, J.M.; Velazquez, O.; Cherry, S.R. Small-Animal X-Ray Dose from Micro-CT. *Mol. Imaging* **2004**, *3*, 149–158. [CrossRef]
23. Hartung, M.P.; Grist, T.M.; François, C.J. Magnetic Resonance Angiography: Current Status and Future Directions. *J. Cardiovasc. Magn. Reason.* **2011**, *13*, 19. [CrossRef]
24. Riederer, S.J.; Haider, C.R.; Borisch, E.A.; Weavers, P.T.; Young, P.M. Recent Advances in 3D Time-Resolved Contrast-Enhanced MR Angiography. *J. Magn. Reason. Imaging* **2015**, *42*, 3–22. [CrossRef]
25. Laub, G. Principles of Contrast-Enhanced MR Angiography: Basic and Clinical Applications. *Magn. Reson. Imaging Clin. N. Am.* **1999**, *7*, 783–795. [CrossRef]
26. Chappell, F.M.; Wardlaw, J.M.; Brazzelli, M.; Best, J.J. Doppler Ultrasound, CT Angiography, MR Angiography, and Contrast-enhanced MR Angiography versus Intra-arterial Angiography for Moderate and Severe Carotid Stenosis in Symptomatic Patients. *Cochrane Database Syst. Rev.* **2017**, *2017*, CD007423. [CrossRef]
27. Scotto di Santolo, M.; Sagnelli, M.; Mancini, M.; Scalvenzi, M.; Delfino, M.; Schonauer, F.; Molea, G.; Ayala, F.; Salvatore, M. High-Resolution Color-Doppler Ultrasound for the Study of Skin Growths. *Arch. Dermatol. Res.* **2015**, *307*, 559–566. [CrossRef]
28. Bercoff, J.; Chaffai, S.; Tanter, M.; Sandrin, L.; Catheline, S.; Fink, M.; Gennisson, J.L.; Meunier, M. In Vivo Breast Tumor Detection Using Transient Elastography. *Ultrasound Med. Biol.* **2003**, *29*, 1387–1396. [CrossRef]
29. Fercher, A.F.; Drexler, W.; Hitzenberger, C.K.; Lasser, T. Optical Coherence Tomography—Principles and Applications. *Rep. Prog. Phys.* **2003**, *66*, 239–303. [CrossRef]
30. Katta, N.; Estrada, A.D.; McElroy, A.B.; Gruslova, A.; Oglesby, M.; Cabe, A.G.; Feldman, M.D.; Fleming, R.D.; Brenner, A.J.; Milner, T.E. Laser Brain Cancer Surgery in a Xenograft Model Guided by Optical Coherence Tomography. *Theranostics* **2019**, *9*, 3555–3564. [CrossRef] [PubMed]
31. Spaide, R.F.; Fujimoto, J.G.; Waheed, N.K.; Sadda, S.R.; Staurenghi, G. Optical Coherence Tomography Angiography. *Prog. Retin. Eye Res.* **2018**, *64*, 1–55. [CrossRef] [PubMed]
32. Liu, B.; Brezinski, M.E. 4.14—Optical Coherence Tomography. In *Comprehensive Biomedical Physics*; Brahme, A., Ed.; Elsevier: Oxford, UK, 2014; pp. 209–226.
33. Xia, J.; Yao, J.; Wang, L.V. Photoacoustic Tomography: Principles and Advances. *Electromagn. Waves* **2014**, *147*, 1–22. [CrossRef]
34. Ku, G.; Wang, L.V. Deeply Penetrating Photoacoustic Tomography in Biological Tissues Enhanced with an Optical Contrast Agent. *Opt. Lett.* **2005**, *30*, 507–509. [CrossRef]
35. Sharma, A.; Srishti, S.; Periyasamy, V.; Pramanik, M. Photoacoustic Imaging Depth Comparison at 532-, 800-, and 1064-Nm Wavelengths: Monte Carlo Simulation and Experimental Validation. *J. Biomed. Opt.* **2019**, *24*, 121904. [CrossRef]
36. Zhou, Y.; Yao, J.; Wang, L.V. Tutorial on Photoacoustic Tomography. *J. Biomed. Opt.* **2016**, *21*, 061007. [CrossRef] [PubMed]
37. Nasiriavanaki, M.; Xia, J.; Wan, H.; Bauer, A.Q.; Culver, J.P.; Wang, L.V. High-Resolution Photoacoustic Tomography of Resting-State Functional Connectivity in the Mouse Brain. *Proc. Natl. Acad. Sci. USA* **2014**, *111*, 21–26. [CrossRef] [PubMed]
38. Ogunlade, O.; Connell, J.J.; Huang, J.L.; Zhang, E.; Lythgoe, M.F.; Long, D.A.; Beard, P. In Vivo Three-Dimensional Photoacoustic Imaging of the Renal Vasculature in Preclinical Rodent Models. *Am. J. Physiol. Ren. Physiol.* **2018**, *314*, F1145–F1153. [CrossRef]
39. Kim, C.; Favazza, C.; Wang, L.V. In Vivo Photoacoustic Tomography of Chemicals: High-Resolution Functional and Molecular Optical Imaging at New Depths. *Chem. Rev.* **2010**, *110*, 2756–2782. [CrossRef]
40. Kim, C.; Cho, E.C.; Chen, J.; Song, K.H.; Au, L.; Favazza, C.; Zhang, Q.; Cobley, C.M.; Gao, F.; Xia, Y.; et al. In Vivo Molecular Photoacoustic Tomography of Melanomas Targeted by Bioconjugated Gold Nanocages. *ACS Nano* **2010**, *4*, 4559–4564. [CrossRef] [PubMed]
41. Xia, J.; Wang, L.V. Small-Animal Whole-Body Photoacoustic Tomography: A Review. *IEEE Trans. Biomed. Eng.* **2014**, *61*, 1380–1389. [CrossRef]
42. Jeon, M.; Kim, J.; Kim, C. Multiplane Spectroscopic Whole-Body Photoacoustic Imaging of Small Animals in Vivo. *Med. Biol. Eng. Comput.* **2016**, *54*, 283–294. [CrossRef] [PubMed]
43. Yao, J.; Xia, J.; Maslov, K.I.; Nasiriavanaki, M.; Tsytsarev, V.; Demchenko, A.V.; Wang, L.V. Noninvasive Photoacoustic Computed Tomography of Mouse Brain Metabolism in Vivo. *NeuroImage* **2013**, *64*, 257–266. [CrossRef]
44. Lin, L.; Hu, P.; Shi, J.; Appleton, C.M.; Maslov, K.; Li, L.; Zhang, R.; Wang, L.V. Single-Breath-Hold Photoacoustic Computed Tomography of the Breast. *Nat. Commun.* **2018**, *9*, 2352. [CrossRef]

45. Kuniyil Ajith Singh, M.; Sato, N.; Ichihashi, F.; Sankai, Y. Clinical Translation of Photoacoustic Imaging—Opportunities and Challenges from an Industry Perspective. In *LED-Based Photoacoustic Imaging: From Bench to Bedside*; Kuniyil Ajith Singh, M., Ed.; Springer: Singapore, 2020; pp. 379–393.
46. Han, S.H. Review of Photoacoustic Imaging for Imaging-Guided Spinal Surgery. *Neurospine* **2018**, *15*, 306–322. [CrossRef]
47. Vainio, M.; Halonen, L. Mid-Infrared Optical Parametric Oscillators and Frequency Combs for Molecular Spectroscopy. *Phys. Chem. Chem. Phys.* **2016**, *18*, 4266–4294. [CrossRef] [PubMed]
48. Hu, S.; Maslov, K.; Wang, L.V. In Vivo Functional Chronic Imaging of a Small Animal Model Using Optical-Resolution Photoacoustic Microscopy. *Med. Phys.* **2009**, *36*, 2320–2323. [CrossRef]
49. Rosset, A.; Spadola, L.; Ratib, O. OsiriX: An Open-Source Software for Navigating in Multidimensional DICOM Images. *J. Digit. Imaging* **2004**, *17*, 205–216. [CrossRef]
50. Kim, J.G.; Xia, M.; Liu, H. Extinction Coefficients of Hemoglobin for Near-Infrared Spectroscopy of Tissue. *IEEE Eng. Med. Biol. Mag.* **2005**, *24*, 118–121. [CrossRef] [PubMed]
51. Constantinescu, G.M. *Comparative Anatomy of the Mouse and the Rat: A Color Atlas and Text*; CRC Press Inc.: London, UK, 2018.
52. Li, Y.; Li, L.; Zhu, L.; Shi, J.; Maslov, K.; Wang, L.V. Photoacoustic Topography through an Ergodic Relay for Functional Imaging and Biometric Application in Vivo. *J. Biomed. Opt.* **2020**, *25*, 1–8.
53. Hu, W.; Ma, H.; Hou, B.; Zhao, H.; Ji, Y.; Jiang, R.; Hu, X.; Lu, X.; Zhang, L.; Tang, Y.; et al. Engineering Lysosome-Targeting BODIPY Nanoparticles for Photoacoustic Imaging and Photodynamic Therapy under Near-Infrared Light. *ACS Appl. Mater. Interfaces* **2016**, *8*, 12039–12047. [CrossRef] [PubMed]
54. Temma, T.; Onoe, S.; Kanazaki, K.; Ono, M.; Saji, H. Preclinical Evaluation of a Novel Cyanine Dye for Tumor Imaging with in Vivo Photoacoustic Imaging. *J. Biomed. Opt.* **2014**, *19*, 090501. [CrossRef]